Emerin oligomerization and nucleoskeletal coupling at the nuclear envelope regulate nuclear mechanics against stress

Anthony Fernandez[1], Markville Bautista[2] and Fabien Pinaud[1,2,3*]

[1]Department of Biological Sciences, University of Southern California, 1050 Child Way, Los Angeles, CA 90089, USA.

[2]Department of Chemistry, University of Southern California, 1050 Child Way, Los Angeles, CA 90089, USA.

[3]Department of Physics and Astronomy, University of Southern California, 1050 Child Way, Los Angeles, CA 90089, USA.

*Correspondence should be addressed to F.P. (pinaud@usc.edu)

ABSTRACT

X-linked Emery-Dreifuss muscular dystrophy (EDMD) results from mutations of the nuclear envelope protein emerin, which participates in nuclear mechanotransductions and maintenance of nuclear shape. To better understand the molecular determinants of EDMD, we probed the membrane diffusion and the nanoscale spatial organization of emerin and some of its clinically relevant mutations, using single molecule tracking and super-resolution microscopy. We show that emerin is distributed as monomers and oligomeric clusters at the inner nuclear membrane and that both its diffusion and its oligomeric state are modified by EDMD-associated mutations. Emerin interactions with lamin A/C, nuclear actin and BAF modulate its mobility and its membrane organization. Measurements in nuclei under stress further indicate that the mechanotransducing function of emerin are coupled to its oligomeric state and that defective formation of emerin oligomers result in aberrant nuclear deformation against forces. These findings place emerin at the center of the molecular processes that regulate nuclear shape remodeling in response to mechanical stress.

INTRODUCTION

Emerin is a conserved inner nuclear membrane (INM) protein that participates in the maintenance of the nuclear architecture by interacting with the nucleoskeletal lamina and elements of the linker of the nucleoskeleton and cytoskeleton (LINC) complex[1, 2]. Emerin also contributes to tethering chromatin at the nuclear envelope by binding the DNA-bridging barrier-to-autointegration factor (BAF)[3] and it regulates the activity of chromatin compaction modulators[4]. Both the nucleoskeleton and the compaction state of chromatin contribute to the mechanical responses of nuclei to forces[5] and emerin is deemed a pivotal actor of mechanotransducing processes at the nuclear envelope[6]. When mutated or absent, emerin causes X-linked Emery-Dreifuss muscular dystrophy (EDMD)[7, 8], a disease part of a larger of group of laminopathies[9] associated with structural perturbations of the nuclear envelope and its underlying lamina. While emerin is ubiquitously expressed, mutations in the *EMD* gene primarily affect cells exposed to extensive mechanical stress, such as skeletal and cardiac muscle cells. Emerin-null muscle tissues display deformed and disorganized nuclei, impaired myogenesis and improper muscle fiber formation, which participate in the muscle wasting and cardiac disease phenotypes of EDMD[10-12]. In non-muscle cells, loss of emerin also leads to altered nuclear envelope elasticity and increased nuclear fragility[13], impaired expression of mechanosensitive genes[14] and enhanced apoptosis after continuous mechanical strain[14]. EDMD phenotypes might stem from both an altered structural integrity of the nuclear envelope and modified gene expression profiles.

The structure of emerin and its binding to various partners have been extensively characterized *in vitro*[1]. Emerin is 254 amino acids (aa) long, with a N-terminal globular LAP2-emerin-MAN1 (LEM, aa: 1-45) domain, followed by a long intrinsically disordered region (IDR, aa: 46-222)[15] and a transmembrane domain close to the C-terminus (aa: 223-234) that allows anchoring to the nuclear envelope. Prominent binding partners of emerin include lamin A/C and lamin B[16-18], actin[19], BAF[20], nesprins and SUN proteins from the LINC complex[21, 22], chromatin modification enzymes and other factors[1]. While binding of emerin to BAF takes place via its structured LEM domain, interactions with other binding partners and emerin self-association[18, 23] are mediated by the IDR. Emerin can indeed oligomerize via regions of the IDR that serve as LEM binding and self-assembly sites between emerin monomers[18], and, *in vitro*, emerin self-association into filamentous structures[24] impact binding to lamin A/C and BAF[18]. Post-translational modifications in the IDR and the LEM domain also influence the oligomerization of emerin and its interactions

2

with binding partners[1, 25, 26]. Phosphorylation of emerin residues Y74 and Y95 are required for lamin A/C recruitment to the LINC complex and nuclear envelope stiffening in response to mechanical stress[27]. Additional post-translational modifications regulate the affinity of the LEM domain to BAF[26] and binding to actin[28]. How emerin organizes at the nuclear envelope and participates in protecting the nucleus against mechanical strains remains unclear.

EDMD often involves frame-shift deletions and nonsense mutations of emerin that effectively ablates expression in cells[29]. Yet, a few sets of point mutations and small deletions, including Δ95-99, Q133H and P183H/T, also cause EDMD despite an apparently correct localization of these mutated emerins at the nuclear envelope and normal cellular expression levels[19, 20, 30, 31]. These emerin mutants, however, display altered self-association and binding to nucleoskeletal proteins[1, 23] and possible changes in molecular organizations at the nuclear envelope might explain why they act as null emerin.

Here, we used super-resolution imaging by stochastic optical reconstruction microscopy (STORM) and single particle tracking by photoactivated localization microscopy (sptPALM) to investigate the nanoscale organization of wild-type emerin and emerin mutants at the nuclear envelope in cells. By modulating the mechanical landscape of nuclei using cell micropatterning techniques[32], we also studied how emerin participates in nuclear envelope mechanotransduction processes during stress. We show that emerin oligomerization and its interactions with key structural partners at the nuclear envelope is central to nuclear shape adaptation against mechanical challenges.

RESULT AND DISCUSSION

Emerin displays distinct diffusive behaviors at the ER and nuclear envelope

To study the nuclear envelope dynamics of wild-type and dystrophy causing mutations of emerin, we made PA-TagRFP-emerin fusions that we expressed in emerin-null human dermal fibroblasts (HDF) from an EDMD patient (*EMD*[-/y])[33]. PA-TagRFP-emerin expression led to the expected localization of emerin at the nuclear envelope, as observed for endogenous emerin in HDF from a healthy individual (*EMD*[+/y]) (Figure 1a). For sptPALM, PA-TagRFP-emerin was excited at 405 nm and 561 nm using highly inclined and laminated optical sheet (HILO)[34] illumination to photoactivate single emerin molecules and image their diffusion at the bottom nuclear envelope.

3

Diffusion tracks were generated from localized emerin appearances (Figure 1b and Supplementary Movie 1) and diffusion analyses were performed using the probability distribution of square displacement (PDSD)[35] to separate unique diffusive behaviors (Figure 1c).

From the PDSD analysis of thousands PA-TagRFP-emerin trajectories, we observed that wild-type emerin exhibits four distinct diffusive behaviors with diffusion values D_1: $2.21 \times 10^{-1} \pm 4.9 \times 10^{-2}$ $\mu m^2/s$, a value similar to that previously reported for diffusion at the ER membrane[36], D_2: $1.48 \times 10^{-2} \pm 1.5 \times 10^{-3}$ $\mu m^2/s$, D_3: $1.73 \times 10^{-3} \pm 1.1 \times 10^{-4}$ $\mu m^2/s$, and D_4: $2.6 \times 10^{-4} \pm 1 \times 10^{-5}$ $\mu m^2/s$ (Figure 1d and Supplementary Table 1). The putative ER population D_1 makes up 1% of the detected behaviors, while the next slowest population D_2 represents 9%, a small fraction of emerin similar to that expected at the outer nuclear membrane (ONM)[2, 6]. The two slowest populations D_3 and D_4 collectively represent 90% of emerin diffusive behaviors. To determine if these four diffusive behaviors are associated with specific positions of emerin at the nuclear envelope, we examined the diffusion coefficient of single emerins from individual mean square displacements. Based on their diffusion coefficients, we grouped emerin trajectories into four diffusion ranges spanning the D values measured from PDSD analyses and plotted them as maps (Figure 1e). In trajectory maps, the fastest emerin population D_1 is primarily distributed in the immediate proximity of nuclear envelope (Figure 1e), a location consistent with diffusion in the ER membrane. The three slower populations D_2, D_3 and D_4 display enrichment at the nuclear membrane (Figure 1e). Compared to diffusion analyses by fluorescence recovery after photobleaching, where we could detect only two diffusive behaviors of wild-type emerin (Supplementary Figure 1), sptPALM measurements show that the mobility of emerin involves four very different types of diffusions at and around the nuclear envelope.

Emerin organizes as slowly diffusing monomers or oligomers at the inner nuclear membrane

Emerin primarily localizes at the INM but a small fraction is often detected at the ONM[2, 6], where it cannot interact with the nuclear lamina. We therefore determined if interactions with lamin A/C would affect specific diffusing populations of wild-type emerin. We found that downregulation of lamin A/C expression by siRNA (Supplementary Figure 2) increases the mobility of the two slowest populations D_3 and D_4 ($p<0.01$, Figure 2a and Supplementary Table 1), but does not affect the faster populations D_1 and D_2 (p not significant, Figure 2a). This indicates that D_3 (40%) and D_4 (50%) are two distinct emerin populations diffusing at the INM and interacting with lamin A/C,

4

while population D_2 (9%) corresponds to emerin diffusing at the ONM. A similar increase in the mobility of emerin populations D_3 and D_4 is also observed when nuclear actin is depleted after downregulating the expression of the actin nuclear import factor, importin-9[37] (IPO9, Supplementary Figure 2), although decreased nuclear actin levels indirectly induce slightly faster emerin diffusion at the ONM (Figure 2a and Supplementary Table 1). These results indicate that a large majority of emerin is organized as two distinct INM pools, both interacting with the nucleoskeleton.

Emerin can also self-assemble *in vitro*[23, 24], and its oligomerization at the INM could result in the slow mobility we observed, in particular if emerin oligomers are tethered by the nucleoskeleton. To determine if diffusing populations D_3 or D_4 correspond to emerin monomers or oligomers, we tracked individual emerins in their dimeric and oligomeric forms. We co-expressed wild-type emerin fusions to self-complementary split-GFP fragments[38] (sGFP-emerin and M3-emerin, Figure 2b) to irreversibly induce the formation of complemented emerin-GFP-emerin species and we studied their lateral mobility by complementation activated light microscopy[39] (CALM). We found that emerin-GFP-emerin species localize almost exclusively at the nuclear envelope (Figure 2c and Supplementary Movie 2), where they diffuse as two separate populations: a dominant 90% population with a mobility similar to D_4 (*p* not significant, Figure 2d), and a minor 10% population with a mobility similar to the ONM population D_2 (*p* not significant, Figure 2d). No fluorescent species with diffusion coefficients matching those of the ER population D_1 or the INM population D_3 are detected. Emerin-GFP-emerin trajectories often spatially overlap, suggesting that emerin forms multimers rather than strictly dimers at the INM (Figure 2c). These results indicate that population D_3 detected by sptPALM but not by CALM represents emerin monomers, while the slowest population D_4 represents dimers or, more likely, larger emerin oligomers at the INM. The nearly 10-fold difference in translational diffusion coefficient between populations D_3 and D_4 is close to the 10-40 fold reduction in mobility reported when monomeric membrane proteins transition to oligomers[40]. The detection of a few emerin-GFP-emerin species at the ONM is likely due to split-GFP-induced emerin dimers that cannot translocate through peripheral nuclear pores channels[9] and do not access the INM.

Emerin monomers and oligomers interact with BAF and diffuse in specific inner nuclear membrane domains

BAF binds the LEM domain of emerin with high affinity[18] and, because it also binds to lamin A/C[41] and chromatin[42], it likely participates in the slow mobility of emerin at the INM[43]. To study how binding of emerin monomers and oligomers to BAF might influence their diffusion, endogenous BAF was knocked down by siRNA (Supplementary Figure 2) and replaced by the expression of BAF L58R, a mutant that does not bind LEM domains[44]. When unable to bind BAF L58R, emerin monomers diffuse significantly faster with a lateral mobility higher than for lamin A/C or IPO9 knock down ($p<0.01$, Figure 2a and Supplementary Table 1). Emerin oligomers also diffuse faster ($p<0.01$, Figure 2a), indicating that BAF modulates the INM dynamics of emerin when it oligomerizes. While emerin diffusion at the ER is undisturbed, its mobility at the ONM increases ($p<0.01$, Figure 2a), suggesting that cytoplasmic BAF additionally interacts with emerin at the ONM. BAF is highly mobile in the nucleus[43] and the comparatively slow mobility of BAF-bound emerin at the INM likely stems from the formation of ternary complexes with lamin A/C or chromatin. The stronger influence of BAF L58R on emerin dynamics compared to lamin A/C depletion indeed suggests that BAF binding modulates the mobility of emerin not only via lamin A/C, but also via interactions with other nuclear components, potentially chromatin.

We additionally built diffusion maps of wild-type PA-tagRFP-emerin at the nuclear envelope by spatial rendering of diffusion coefficients at the position of each tracked molecule (Figure 2e). Those maps are dominated by the two slowest INM emerin populations, which represent 90% of the total pool detected. They show that domains with very slow diffusion and attributed to emerin oligomers, are distributed throughout the nuclear envelope and are surrounded by diffusion areas where the mobility of emerin is faster and matches that of monomers (Figure 2e). This suggests a membrane-wide, yet locally structured distribution of emerin at the INM, with monomers surrounding emerin oligomer domains in an organization compatible with emerin monomer/oligomer exchanges in distinct INM areas.

Together, these diffusion analyses indicate that the membrane mobility of emerin is complex. Newly synthesized emerin diffuse rapidly at the ER membrane on their way to the juxtaposed ONM, where emerin diffusion is slower, in part by interaction with cytoplasmic BAF. Once at the INM, the mobility of emerin is further reduced, with emerin monomers and oligomers interacting

with nuclear BAF and the nucleoskeleton. This distribution is consistent with a combined BAF-induced and lamina-induced retention and accumulation of emerin at the INM.

Emerin forms oligomeric nanodomains surrounded by monomers

We then probed the structural organization of emerin in more detail using super-resolution microscopy. Wild-type emerin fused to a SNAP-tag (SNAP-emerin) was expressed in $EMD^{-/y}$ HDF and, after chemical fixation, cells were stained with benzylguanine-AlexaFluor647 to image individual emerins by dSTORM (Figure 3a). An emerin neighborhood density function (NDF) built from localized emerin positions across multiple nuclei was compared to MonteCarlo simulations of completely random distributions and fitted with exponential decay models[45] to measure molecular densities and length scales of significant clustering. We found that wild-type emerin is not distributed randomly at the nuclear envelope, as it displays density distributions significantly higher than expected for a completely random organization (Figure 3b). The NDF curve is best fitted with a two exponential decay model, indicating that emerin organizes into two distinct clustering states across the nuclear envelope. The first type of cluster is small with a typical cluster length of 22±11 nm and a molecular density of emerin 8.2±0.2 fold higher than expected for a random distribution (Figure 3c and Supplementary Table 2). The second type of cluster is significantly larger with a typical cluster length of 236±30 nm and an emerin density slightly above the expected value of 1 for complete randomness (1.3±0.1 fold, Figure 3c). In cluster maps built from local cluster analyses[46], wild-type emerin forms small high density clusters that are scattered throughout the nuclear envelope and are surrounded by larger emerin areas with densities close to random (Figure 3d). These cluster maps are strikingly similar to our sptPALM diffusion maps in live cells (Figure 2e) and indicate that small, high emerin density clusters are oligomers while the surrounding larger areas are populated by emerin monomers. While it is intriguing that emerin monomers appear as slightly clustered, a fully random distribution is not to be expected because they do not populate membrane-less areas of the nuclear envelope, such as nuclear pores. These observations confirm that, across the INM, emerin organizes into small and discrete oligomeric units surrounded by dispersed monomers.

Emerin oligomers are primarily stabilized by lamin A/C and partially maintained by nuclear actin and BAF

We then determined the importance of lamin A/C, nuclear actin and BAF in maintaining the spatial organization of emerin at the INM. Wild-type emerin was imaged by super-resolution microscopy after siRNA knock down of lamin A/C, IPO9, or replacement of endogenous BAF with BAF L58R. After lamin A/C depletion, the molecular density of emerin is dramatically reduced at all length scales (Figure 3b). The NDF distribution is comprised of small, 35±17 nm emerin clusters with molecular density close to random (1.2±0.1 fold, Figure 3c and Supplementary Table 2) and of large 950±173 nm emerin monomer domains with density just above random (1.1±0.1 fold, Figure 3c). Compared to emerin distributions in cells having normal lamin A/C levels, emerin monomers are dispersed over larger areas and, importantly, emerin oligomers nearly vanish. Such changes in organization are seen in emerin cluster maps of lamin A/C depleted nuclei, where most oligomeric nanodomains have dissipated, and where monomers cover a significantly larger part of the nuclear envelope (Figure 3d). This indicates that lamin A/C plays an important structural role for the stabilization of emerin oligomers and the general spatial distribution of emerin monomers at the INM.

When nuclear actin is depleted after knocking down of IPO9, wild-type emerin forms oligomers having a reduced molecular density of 3.6±0.1 fold above random and a larger size of 65±13 nm compared to untreated cells (Figure 3c and Supplementary Table 2). Emerin monomers are dispersed over membrane domains having a typical length scale of 382±81 nm, which is larger than in untreated cells (236±30 nm, Figure 3c), but not as large as for lamin A/C knock down (950±173 nm, Figure 3c). Thus, despite reduced nuclear actin levels, emerin retains the ability to oligomerize, although it disperses over large INM areas. These results indicate that, together with lamin A/C, nuclear actin contributes to maintaining the overall spatial distribution of emerin at the INM and additionally participates in the structural maintenance of emerin oligomers, albeit to a lesser degree than the lamina itself.

When endogenous BAF is replaced by BAF L58R, wild-type emerin oligomers are still formed but they have a reduced molecular density of 2.0±0.1 fold above random and a larger size of 85±19 nm compared to cells expressing wild-type BAF (Figure 3c and Supplementary Table 2). The inability to bind BAF also induces a re-distribution of emerin monomers over large INM domains with typical sizes of 718±250 nm (Figure 3c). Consistent with our diffusion results, emerin binding

to BAF modulates the organization of both oligomerizic and monomeric emerin and strongly influences the spatial distribution of emerin monomers at the INM.

Together, these results show that wild-type emerin monomers are distributed throughout the INM where their dispersion is maintained by direct binding to BAF and additional spatial constrains imposed by lamin A/C and nuclear actin. Emerin additionally organizes into discrete and small oligomeric nanodomains that are surrounded by monomers and are structurally stabilized by lamin A/C and, to a lesser or more indirect extent, by BAF and nuclear actin.

Increased diffusion of emerin monomers and oligomerization upon nuclear adaptation to mechanical stress

We then sought to define the mechanotransducing functions of emerin by studying how its diffusion and its nanoscale organization change when nuclei are subjected to increasing mechanical stress. SptPALM and super-resolution imaging of wild-type emerin were done in $EMD^{-/y}$ HDF grown on increasingly narrow rectangular micropatterns with widths of 15 µm, 10 µm or 5 µm, to impose steady-state mechanical stress to the nucleus[6, 32, 47] (Figure 4a and 4b). First, we verified that changes in nuclear shape index (NSI) on these micropatterns reflect the mechanical adaptation of nuclei against forces by depleting lamin A/C or nuclear actin, two key nucleoskeletal proteins involved in maintaining nuclear shape during stress. In non-patterned cells, nuclei are slightly more deformed after lamin A/C knock down or nuclear actin depletion compared to controls ($p<0.01$, Figure 4c). These effects are further amplified on micropatterns where nuclei become increasingly deformed as patterns get narrower ($p<0.01$, Figure 4c). This indicates that cell micropatterning elicits increased nuclear stress and effectively induces mechanical responses of the nucleus that implicate the nucleoskeleton.

When we tracked wild-type PA-tag-RFP-emerin on deformed nuclei in 15 µm and 10 µm patterns (Supplementary Movie 3), we found that its ER mobility is unchanged compared to non-patterned cells (p not significant, Figure 4d and Supplementary Table 1), while its ONM diffusion is faster ($p<0.01$, Figure 4d). At the INM, emerin monomers also diffuse significantly faster ($p<0.01$, Figure 4d) and the mobility of oligomers increases compared to non-patterned cells, albeit short of statistical significance for 15 µm patterns (p not significant and $p<0.01$, Figure 4d). Interestingly, there is no significant difference in the mobility of all four ER, ONM and INM emerin populations in both types of micropatterns compared to nuclear actin depletion (p not

9

significant, Supplementary Figure 3). These results suggest that nuclear shape adaptation to mechanical cues entails modified interactions of emerin with nuclear actin, notably for monomers. Super-resolution imaging and spatial distribution analyses of wild-type SNAP-emerin further indicate that, as the NSI decreases, monomers disperse over increasingly large INM domains with sizes of $382{\pm}62$ nm and $460{\pm}136$ nm, compared to $236{\pm}30$ nm for non-deformed nuclei (Figure 4e). Concurrently, oligomer densities drop from $8.2{\pm}0.2$ fold to $3.6{\pm}0.1$ fold above random in 15 µm patterns, before increasing slightly to $4.6{\pm}0.1$ fold above random in 10 µm patterns (Figure 4e). Remarkably, oligomeric nanodomains become larger during nuclear stress and their size expands from $22{\pm}11$ nm to $60{\pm}13$ nm in both micropatterns (Figure 4e). When considering this wider spatial distribution of oligomers, the relative oligomerization of emerin compared to non-deformed nuclei increases by 3.4 fold and by 4.1 fold as the nucleus adapts to incremental mechanical stress (Figure 4f). This indicates that nuclear shape adaptation to forces is associated with a gradual change in the oligomerization potential of emerin at the INM. This enhanced oligomerization of emerin over larger nanodomains is likely triggered by nucleoskeletal re-arrangements, because it is accompanied by a faster lateral mobility of emerin. Indeed, the stress-induced spatial reorganizations of emerin in micropatterns, including oligomer densities and emerin domain sizes, is strikingly similar to that observed when nuclear actin is depleted in non-patterned cells (Supplementary Figure 3 and Supplementary Table 2). This suggests that nuclear shape deformation involves a disengagement of nuclear actin from the nucleoskeleton, that leads to a faster diffusion of emerin monomers and to their increased oligomerization. An increased lateral mobility of emerin at the INM could indeed facilitate molecular collisions between monomers and the formation of oligomers stabilized by lamin A/C.

Together, these results indicate that the mechanotransducing functions of emerin are coupled to its oligomeric state along the INM and are modulated by emerin interactions with nucleoskeletal partners, including nuclear actin, in order to ensure appropriate nuclear deformation and response to mechanical challenges.

EDMD emerin mutants induce abnormal nuclear deformation against mechanical stress

To establish the biological significance of emerin oligomerization at the INM and its importance for nuclear adaptation to mechanical stress, we then compared the organization of wild-type emerin with that of mutated forms of emerin known to induce EDMD. We studied how emerin

mutation Q133H, deletion Δ95-99, and mutation P183H (Figure 5a) impact the lateral diffusion and the nanoscale distribution of emerin at the nuclear envelope. First, we verified that mutated emerins effectively induce defective mechanical responses of nuclei when expressed in $EMD^{-/y}$ HDF and we compared changes in NSI after random cell plating or plating on increasingly narrow rectangular micropatterns (Figure 5b, c). In randomly plated cells expressing mutated emerins, nuclei are slightly less circular compared to cells expressing wild-type emerin (Figure 5b). With increasing mechanical stress in micropatterns, cells expressing emerin mutants display significantly higher NSI values than wild-type (Figure 5b), indicative of a failure to correctly modify the shape of the nucleus in response to forces. These deficient changes in nuclear shape are accompanied by a mispositioning of the nucleus relative to the cell major axis, nucleus crumpling, abnormal organization of the actin cytoskeleton and failure of cells to properly fit within micropatterns, specifically in cell areas adjacent to the misshaped nucleus (Figure 5c). It indicates that expression of mutated emerin in $EMD^{-/y}$ HDF prevents nuclear adaptation to mechanical stress, as often observed in muscle cells from EDMD patients[48].

EDMD-inducing emerin mutants display defective oligomerization at the inner nuclear membrane

Q133H mutation

Using sptPALM and super-resolution imaging, we then characterized the nuclear envelope dynamics of each mutated emerin and their respective nanoscale organization, starting with Q133H emerin. We found that the lateral mobility of Q133H PA-TagRFP-emerin is similar to that of wild-type emerin at the ER and the ONM (p not significant, Figure 6a and Supplementary Table 1). However, both Q133H monomers and oligomers diffuse significantly faster at the INM ($p<0.01$ and $p<0.05$, Figure 6a). The Q133H mutation disrupts emerin binding to actin[49] but does not impede interactions with lamin A/C[31], BAF or other partners[50]. The increased lateral diffusion of Q133H, only at the INM, therefore suggests that it does not bind nuclear actin. This faster INM diffusion of Q133H also resembles the increased mobility of wild-type emerin when nuclear actin is depleted (Figure 2a), which further underlines that nucleoskeletal actin modulates the diffusion of emerin monomers and oligomers. This is consistent with previous observations that emerin expression influences the mobility of nuclear actin[51] and indicative of a reciprocal effect of emerin/nuclear actin interactions on their respective mobility. We also noticed that the diffusion

of Q133H at the INM is similar to that of wild-type emerin under mechanical stress, in both 15 µm and 10 µm wide micropatterns (*p* not significant, Supplementary Figure 4 and Supplementary Table 1). This suggests that nuclear deformations against stress involve an initial dissociation of emerin from nuclear actin that leads to faster emerin diffusion at the INM.

Although, it was reported that Q133H has a reduced capacity to self-assemble *in vitro*[23], our analyses of its spatial distribution and cluster maps show that, like wild-type emerin, it organizes into monomers and oligomers across the INM (Figures 6b and 6c). Q133H monomers are distributed over length scales of 213±62 nm, similar to those of wild-type emerin (Figure 6b), indicating that the inability to bind the nuclear actin induces a faster diffusion of Q133H monomers, but does not affect their overall spatial distribution at the INM. Q133H also retains the ability to self-assemble at the INM where it forms oligomeric clusters (Figure 6c). These oligomers have sizes of 19±12 nm, similar to the 22±11 nm size of wild-type emerin oligomers, but they have molecular densities 12.2±0.2 fold above random, a 50% increase in oligomerization compared to wild-type emerin (Figure 6b and Supplementary Table 2). This indicates that the deficient binding of Q133H to nucleoskeletal actin leads to a disproportionate self-association of emerin into oligomeric nanodomains. It also suggests that direct binding to nuclear actin normally reduces the oligomerization potential of wild-type emerin.

Compared to emerin, actin is relatively large and its binding to the IDR of emerin could mask disordered interaction domains that normally serve as LEM binding and self-association sites between emerin monomers[18]. IDR masking, combined with the reduced lateral mobility of actin-bound emerin, might therefore modulate the formation of oligomers by limiting molecular collisions between emerin monomers. Indeed, increased emerin diffusion by unbinding of nuclear actin and enhanced emerin oligomerization at specific sites across the INM appear to be coupled events important for nuclear shape adaptation against stress, as our measurements in micropatterns suggest. The abnormal nuclear deformation of cells expressing Q133H (Figure 5c) might therefore stem from a local over-oligomerization of emerin at the INM and a defective reorganization of nucleoskeletal actin and the neighboring lamina at the nuclear envelope.

Δ95-99 mutation

When we performed similar studies with Δ95-99 emerin, we found that its diffusion at the ER membrane and the ONM is similar to that of wild-type emerin (*p* not significant, Figure 6d and

Supplementary Table 1). However, its lateral mobility at the INM is significantly reduced ($p<0.05$ and $p<0.01$, Figure 6d). This suggests that Δ95-99 interacts more strongly or more frequently than wild-type emerin with some of its binding partners on the nucleoplasmic side of the nuclear envelope. Previous biochemical studies have shown that the small Δ95-99 deletion eliminates emerin interactions with most of its binding partners, including lamin A/C and actin, but not BAF[1]. Considering that binding BAF strongly influences the mobility of wild-type emerin (Figure 2a), the reduced diffusion of Δ95-99 at the INM could stem from its increased interaction with BAF, as recently proposed[24]. To destabilize these interactions, we attempted to track Δ95-99 in *EMD*[-/y] HDF knocked down for endogenous BAF and expressing BAF L58R. Co-expression of both Δ95-99 and BAF mutants, however, proved toxic to cells, suggesting that interactions between Δ95-99 emerin and BAF are important to maintain cell viability.

Beside a slower emerin mobility at the INM, the Δ95-99 deletion also induces defective oligomerization. Δ95-99 is distributed randomly over large, 420±51 nm nuclear envelope domains and in smaller, 48±14 nm nanodomains where the molecular density of 1.3±0.1 fold above random is dramatically reduced compared to wild-type emerin oligomers (Figure 6e and Supplementary Table 2). In cluster maps, Δ95-99 also displays less dense and fewer oligomerization nanodomains (Figure 6f). This indicates that Δ95-99 does not efficiently oligomerize at the INM, consistent with its impaired self-assembly *in vitro* and observations that the deletion lowers emerin/emerin proximity at the nuclear envelope[23]. Interestingly, despite an intact lamina, the molecular densities and cluster maps of Δ95-99 are similar to those of wild-type emerin when the expression of lamin A/C is reduced (Figure 3c, d). The decreased oligomerization of Δ95-99 to levels seen after lamin A/C depletion suggests that binding to lamin A/C is required to stabilize emerin oligomers at the INM. Such a stabilizing role of lamin A/C is consistent with prior proximity ligation assays where Δ95-99 was found less close to lamin A/C than wild-type emerin at the nuclear envelope[23] and studies showing that the deletion abolishes lamin A/C binding to emerin[20].

Together, these results indicate that Δ95-99 fails at oligomerizing and primarily distributes at random throughout the INM due to its reduced self-association, its inability to directly bind lamin A/C and its slow mobility, which we propose is linked to an increased binding frequency to BAF. The 48-118 region of emerin, where Δ95-99 is located, was suggested to act as a potential binding site for the LEM domain[18] and through altered region flexibility, the deletion might reduce the efficacy of such interactions, potentially causing the LEM domain to bind BAF more frequently.

13

Repeated interactions of Δ95-99 with BAF and indirectly with the lamina, via BAF binding to lamin A/C[41], could slow diffusion, limit molecular collisions, and impede oligomerization by sequestering the LEM domain and reducing its bridging interactions with LEM binding sites on other emerins[18]. The Δ95-99 deletion, within the 55-132 lamin tail-binding region of emerin[18], could further prevent a stabilization of already sparse Δ95-99 oligomers by lamin A/C. The aberrant nuclear deformation against stress observed for cells expressing Δ95-99 (Figure 5c) likely stems from out of balance interactions of the deletion mutant with BAF and its inability to form lamin A/C-stabilized oligomers.

P183H mutation

SptPALM tracking of P183H emerin reveals that its lateral diffusion at the ER membrane and the ONM is unchanged compared to wild-type emerin (*p* not significant, Figure 6g and Supplementary Table 1). However, its mobility at the INM is reduced for the populations attributed to monomers and oligomers ($p<0.05$ and $p<0.01$, Figure 6g). This slow diffusion is similar to that observed for Δ95-99 and again suggests that P183H interacts more frequently than wild-type emerin with some of its nucleoplasmic binding partners. *In vitro*, P183H maintains its binding to many emerin partners, including BAF and actin[1] and displays enhanced binding to lamin A/C compared to wild-type emerin[1, 20]. The observed reduced INM diffusion of P183H might therefore be linked to an increased binding frequency to BAF, like for Δ95-99, or to its enhanced binding to lamin A/C. Alternatively, this slow INM mobility could be due to the formation of dimers as recently suggested based on the strong propensity of P183H to self-assemble *in vitro*[23] and observations that residue P183 is positioned in the 168-186 emerin region required to limit emerin-emerin association[18]. To determine if P183H tends to form dimers at the nuclear envelope, we performed single particle tracking by CALM after co-expression of sGFP-P183H and M3-P183H emerin. Three different populations of fluorescently activated P183H-GFP-P183H emerin species were detected at the nuclear envelope: a 2% population with a mobility slightly slower than P183H at the ER membrane ($p<0.05$, Figure 6g), a larger 39% population with a mobility comparable to the ONM behavior of P183H (*p* not significant, Figure 6g), and a dominant 59% population with a lateral diffusion similar to the INM population initially attributed to P183H monomers by sptPALM (*p* not significant, Figure 6g and Supplementary Table 1). Surprisingly, no fluorescent species with diffusion coefficient matching that of the slowest P183H oligomers are detected

14

(Figure 6g). The high frequency detection of complemented split-GFP for P183H compared to wild-type emerin at the ER membrane and the ONM (Figure 2d) indicates that P183H is more prone to self-assemble and to form dimers than wild-type emerin before reaching the INM. This apparent biased monomer:dimer equilibrium towards dimers is maintained at the INM where it precludes an efficient association of P183H into oligomer domains, in particular when dimers are further stabilized by irreversible assembly of the split-GFP fragments. This suggests that P183H has a propensity to form dimers that could impact oligomerization at the INM.

Consistent with these observations, spatial analyses reveal that the dimerization of P183H leads to a significantly reduced oligomerization at the INM. P183H monomers/dimers are distributed in domains with typical sizes of 321±29 nm and molecular densities of 1.3±0.1 fold above random (Figure 6h and Supplementary Table 2). Smaller nanodomains with sizes of 35±12 nm are also observed, but their molecular density is reduced to 2.2±0.1 compared to wild-type emerin oligomers (Figure 6h). This indicates that the dimerization of P183H hinders further self-association into denser oligomers at the INM. Indeed, while P183H can still bind lamin A/C, it forms oligomeric domains having lower molecular density than wild-type emerin in cluster maps (Figure 6j). The reduced ability of P183H to oligomerize could stem from a limited access of the LEM domain to self-association sites along the joined IDR of P183H dimers, impeding *in trans* interactions. The reported enhanced binding of lamin A/C in close proximity to these same sites might similarly interfere with inter-emerin bridging interactions. In both cases, the inability of the LEM domain to access binding sites along the IDR could elicit its repeated interactions with BAF, leading to the observed slow diffusion of P183H at the INM. The defective nuclear shape adaptation to mechanical challenges of cells expressing P183H (Figure 5c) might therefore stem from emerin dimerization and excessive interactions with BAF or lamin A/C that prevents an efficient formation of emerin oligomers and a remodeling of the nucleoskeleton.

Abnormal reorganization of Δ95-99 emerin in response to mechanical stress

To further characterize the importance of emerin oligomerization for nuclear deformation and responses to mechanical stress, we studied the nanoscale organization of Δ95-99 in micropatterned cells. For deformed nuclei in 15 µm patterns, Δ95-99 monomers are dispersed over large, 810±215 nm INM domains, almost double the size of monomer domains in non-stressed nuclei (420±51 nm, Figure 7a). However, as abnormal nuclear deformations become more pronounced in 10 µm

patterns, the distribution of Δ95-99 monomers return to non-stress levels, with dispersions in domains 499±250 nm in size (Figure 7a). Contrary to wild-type emerin, a progressive dispersion of Δ95-99 monomers over increasingly large INM areas is not observed with growing stress. At the same time, the formation of oligomers remains very limited, with Δ95-99 molecular densities increasing slightly from 1.3±0.1 to 1.7±0.1 and 2.0±0.1 fold above random for 15 µm and 10 µm micropatterns (Figure 7a and Supplementary Table 2). With the concurrent size enlargement of nanodomains from 48±14 nm to 81±16 nm and 75±20 nm, the relative oligomerization of Δ95-99 compared to non-mechanically stressed nuclei increases by 3.9 fold initially, but does not rise further as nuclear stress intensifies (Figure 7b). Despite this modest increase, Δ95-99 oligomeric nanodomains remains sparser and significantly less dense than for wild-type emerin in cluster maps of nuclei under stress (Figure 7c). Thus, compared to wild-type emerin, the failure of Δ95-99 to gradually self-associate at sufficiently high molecular densities leads to defective nuclear responses to force and underlines the importance of modulating the oligomerization of emerin as a function of mechanical stress for adaptive nuclear deformations.

The phosphorylation of emerin residues Tyr 74 and Tyr 95 by Scr kinase[52] was recently shown to mediate the recruitment of lamin A/C to the LINC complex during nuclear stiffening in response to force[27]. Our observation that Δ95-99 fails at promoting normal nuclear deformation against mechanical stress by its inability to form lamin A/C-stabilized emerin oligomers is consistent with the major role played by Tyr 95 phosphorylation for emerin-mediated mechanotranslation at the nuclear envelope. The abnormal organization of cytoskeletal actin in mechanically challenged cells expressing Δ95-99 (Figure 5c), akin to disorganizations observed with a non-phosphorylable tyrosine 74-95FF emerin mutant[27], also suggests that emerin oligomers are required to strengthen the connection between lamin A/C, the LINC complex and cytoplasmic actin filaments in order to promote correct nucleus positioning and deformation. This points towards a link between Tyr 95 phosphorylation, emerin oligomerization and recruitment of lamin A/C for stiffening the nuclear envelope at LINC complexes, that could be driven by phosphorylation-induced changes in emerin conformation and binding to nuclear partners[26, 27, 52]. It is thus possible that oligomeric nanodomains at the INM are enriched in Tyr 95 phosphorylated emerin, lamin A/C and LINC complex components, while emerin monomers populate the rest of the INM, consistent with emerin enrichments in distinct nucleoskeletal "niches" at the nuclear envelope[26].

CONCLUSION

Using a combination of single molecule imaging and quantitative measurements, we showed that emerin is distributed as monomers and oligomers at the INM and that clinically relevant EDMD mutations induce modified emerin mobility and nanoscale organizations. The oligomerization of emerin at specific sites across the nuclear envelope is modulated by its ability to engage or disengage interactions with different structural elements juxtaposed to the INM, including lamin A/C, nuclear actin and BAF. Lamin A/C is essential for a stabilization of emerin oligomers and balanced interactions of emerin with BAF and nuclear actin are further required to modulate its diffusion and its oligomerization potential. We also observed that mechanotransducing functions of emerin are coupled to its the oligomeric state, with the formation, stabilization and maintenance of emerin oligomers being central to nuclear shape adaptation to forces. Indeed, EDMD-inducing mutations that affect the oligomerization of emerin and its binding to structural elements at the INM lead to abnormal nuclear deformation and defective nuclear positioning in response to mechanical stress.

While the altered *in vitro* binding properties of Q133H, Δ95-99 and P183H emerin mutants result in expected differences in organization *in vivo*, they do not necessarily induce fully predicable changes in diffusion and distribution at the nuclear envelope. In effect, via its flexible IDR, emerin appears to mediate complex interactions with itself, lamin A/C, nuclear actin and BAF, where binding to one partner impacts oligomerization and, interdependently, affects interactions with other partners.

We propose that, during stress responses, transient unbinding of emerin monomers from BAF and nuclear actin favors oligomerization by increasing lateral diffusion at the INM and exposing both the LEM domain and self-association sites along the IDR for intermolecular binding between emerins. Within emerin oligomers, stabilization by direct interaction with the lamin A/C and additional modulation of emerin self-association by nuclear actin and BAF likely allow for a fine regulation of the oligomerization potential and the size of oligomeric domains, as required for adaptive nuclear deformation in response to forces. The localized INM distribution of emerin oligomers and their reliance on a part of the emerin IDR that requires phosphorylation for the recruitment of lamin A/C to the LINC complex[27], also suggest that they are sites where interactions between emerin, lamin A/C and LINC components are strengthened. Emerin oligomerization might therefore contribute to the increased connectivity between the nucleoskeleton, the nuclear

17

envelope and the cytoskeleton for anchoring the nucleus and for providing force absorption contact points during nuclear deformation. In response to surging mechanical stress, the incremental oligomerization of emerin in larger nanodomains we observed could be part of a mechanism that redistributes increasing forces over wider areas to maintain a basal membrane pressure at local anchoring points between the nucleoskeleton, the nuclear envelope and the cytoskeleton. Outside these anchoring oligomeric domains, disengagement of emerin monomers from nuclear actin likely provides additional modulations of nucleoskeletal contacts with the nuclear envelope, for instance by reducing the connections of the INM with the nucleoskeleton, while maintaining its connectivity with nuclear chromatin, via BAF. Indeed, both tethering of chromatin to the nuclear envelope and the nucleoskeleton participate in nuclear mechanics[5, 53]. Together, strengthening the connections between the nuclear envelope and the lamina at specific cytoskeletal anchor points, but relaxing them in the rest of the membrane could provide a means to couple controlled nuclear deformation with nucleus positioning in cells. Such coupling is defective with emerin mutants, which display abnormal oligomerization and modified interactions with nucleoplasmic partners. The structural interdependency between emerin monomers, emerin oligomers, BAF, and key elements of the nucleoskeleton likely provides an integrated mechanism where INM/lamina contacts and INM/chromatin contacts are spatially regulated and where reinforced connectivity between the nuclear envelope and the cytoskeleton is provided where needed. At the center of such processes, emerin diffusion and monomer/oligomer exchanges ensure that mechanical cues are transduced throughout the nuclear envelope, for coordinated changes in local nuclear stiffness and appropriate remodeling of the nuclear shape.

METHODS

Cell culture, emerin expression and cell staining

Emerin-null human dermal fibroblast (*EMD*$^{-/y}$ HDF) and normal dermal fibroblasts (*EMD*$^{+/y}$ HDF) were kindly provided by Dr. Howard Worman, Columbia University, New York, USA. *EMD*$^{-/y}$ HDF are derived from a male EDMD patient (G-9054) and carry a 59 nucleotide deletion within the *EMD* gene (*EMD* g.329del59) that ablates emerin expression[22]. HDF were grown in DMEM (Lonza) with 10% fetal bovine serum (Gibco-Life Technologies), 50 units/ml penicillin and 50 µg/ml streptomycin and maintained at 37°C in a humidified atmosphere with 5% CO_2.

Human wild-type emerin cDNA was kindly provided by Dr. Juliet Ellis, University College London, UK. For the expression of PA-TagRFP-emerin, a pEGFP-N1 plasmid backbone encoding emerin fused to the C-terminus of PA-TagRFP was produced by XbaI and KpnI insertion and PCR fusion of the human emerin cDNA. Cells plated on fibronectin-coated glass coverslips were

transfected with PA-TagRFP-emerin using X-tremeGENE HP (Roche). 48-72 hours post-transfection, live cells were imaged by sptPALM in HBSS buffer at 37°C. For micropatterning experiments, cells grown on 6-well plates were trypsinized after 48-72 hours of transfection and plated on fibronectin-micropatterned coverslips.

To express SNAP-emerin, human emerin was first fused to the C-terminus of a SNAP tag by AscI and XhoI insertion in a pSNAP-tag(m) plasmid (NEB). SNAP-emerin was then subcloned into a modified pFUW lentiviral vector by NheI and AgeI insertion. Lentiviral particles for the expression SNAP-emerin were produced by the UCLA Vector Core. Transduction of HDF grown at 70% confluence on 6-well plates was done for 48 hours, using 25 ng/ml of lentiviral particles in complete growth medium containing 8 μg/ml of polybrene, after which the medium was replaced. Following another 24 hours incubation, cells were trypsinized, and plated on fibronectin-coated or fibronectin-micropatterned coverslips. For imaging, cells were fixed with 4% paraformaldehyde in PBS for 15 min, permeabilized with 0.1% Triton X-100 (Sigma-Aldrich) for 15 min and blocked with 4% bovine serum albumin (BSA, Sigma-Aldrich) + 0.1% Tween-20 (Sigma-Aldrich) for 30 min, at room temperature. Cells were then stained with 1 μM of SNAP-Surface-AlexaFluor 647 (BG-A647, NEB) in 4% BSA + 0.1% Tween-20 for 1 hour at 37°C, then thoroughly washed before super-resolution imaging.

For the expression of sGFP-emerin, humanized cDNA for split-GFP 1-10[39] was inserted by NheI and XbaI digestion in the pEGFP-N1 plasmid backbone encoding emerin, and expressed as an N-terminal fusion to emerin. The shorter 11th β-sheet M3 fragment[39] was also fused to the N-terminus of emerin by PCR cloning using primers encoding the M3 fragment sequence and subcloning into the pEGFP-N1 backbone via NheI and XhoI digestions. Both plasmids were co-transfected in HDF using X-tremeGENE HP (Roche) as described for PA-TagRFP-emerin, and cells were imaged by CALM 48-72 hours post-transfection. All constructs were verified by sequencing. Upon re-expression of wild-type emerin fusions in $EMD^{-/y}$ HDF, nuclear deformations against mechanical stress recover to levels similar to those of normal $EMD^{+/y}$ HDF[47].

For immunostaining of emerin, cells were grown on coverslips, fixed and permeabilized as described for SNAP-emerin staining. Cells were labeled with a rabbit anti-emerin antibody (1:500, Santa Cruz Biotechnology, sc-15378) for 45 min, washed in PBS and further labeled with a goat anti-rabbit Alexa fluor 488 antibody (1:400, Invitrogen) for 45 min. After washing, cells were mounted in a DAPI-Fluoromount G (Electron Microscopy Sciences) and imaged by confocal microscopy.

To label cytoplasmic actin and measure nuclear shape indices, cells were fixed with 4% paraformaldehyde in PBS for 15 min, permeabilized with 0.1% Triton X-100 for 10 min, and blocked with 4% bovine serum albumin + 0.1% Tween-20 for 1 hour. Cells were stained with phalloidin-iFluor 488 (1:1000, Abcam) for 1 hour, washed with PBS, mounted in DAPI-Fluoromount G and imaged by confocal or wide field microscopy.

Mutations, siRNA and BAF L58R expression

Emerin mutations Q133H and P183H were introduced in PA-TagRFP-emerin, SNAP-emerin, sGFP-emerin and M3-emerin by site-directed mutagenesis using QuickChange Lightning Site Directed Mutagenesis (Agilent) and mutagenic primer pairs for:

Q133H: 5'-CGCTTTCCATCACCATGTGCATGATGA-3' and
          5'-GATCGTCATCATGCACATGGTGATGGA-3'

P183H: 5'-CCTGTCCTATTATCATACTTCCTCCTC-3' and
          5'-GTGGAGGAGGAAGTATGATAATAGGA-3'.

19

The Δ95-99 emerin deletion was produced using partially phosphorothioated PCR primers and T7 exonuclease digestion, as previously described[54]. Primers pairs for the Δ95-99 deletion were:

5'-GACTACTTCACCA*C*C*A*GGACTTAT-3' and
5'-GGTGAAGTAGTCG*T*C*A*TTGTAGCC-3',

where * denotes phosphorothioate modifications. All primers were obtained from Integrated DNA Technologies (IDT) and all mutations were verified by sequencing.

siRNA duplex for BAF and Dicer siRNA for lamin A/C were obtained from IDT. The sequences of sense nucleotides were as follows: BAF siRNA: 5'-AGAUUGCUAUUGUCGUACUUU-3', lamin A/C DsiRNA: 5'-AGCUGAAAGCGCGCAAUACCAAGaa-3'. siRNA duplex for IPO9 was obtained from Ambion (id # S31299). All siRNA were transfected or co-transfected with emerin plasmids at 25 nM using X-tremeGENE HP (Roche). When associated with lentiviral expression of emerin, siRNA transfection was done 2 hours before viral titer application.

BAF L58R was expressed from an EGFP-BAF L58R lentiviral plasmid[44] (Addgene #101776) and lentiviral particles were produced by the UCLA Vector Core. HDF cells were transduced with 25 ng/ml of lentiviral particles as described for SNAP-emerin.

Cell micropatterning and nuclear shape index measurements

HDF were micropatterned as described previously[32, 47]. Briefly, hexamethyldisilazane-activated glass coverslips (Marienfeld, #1.5, Ø25 mm) were stamped with rectangular and fibronectin-coated polydimethylsiloxane stamps having lengths of 210 µm and widths of 15 µm, 10 µm, or 5 µm respectively. Cell attachment outside the fibronectin strips was blocked with a 1% solution of Pluronic F-127. After attachment for 1 hour and removal of unattached cells, HDF were allowed to spread out on the micropatterns for 6 hours at 37°C before being prepared for microscopy imaging.

Using ImageJ[55], the nuclear shape index (NSI)[56] was determined by measuring the nuclear cross-sectional area and the nuclear perimeter of DAPI-stained nuclei imaged by wide-field microscopy, and by calculating the ratio:

$$\text{NSI} = \frac{4 \times \pi \times \text{area}}{\text{perimeter}^2} \qquad (1)$$

The NSI measures the roundness of the nucleus with an NSI of 1 corresponding to a circular nuclear shape. Mean NSI values ± standard deviation of the mean are reported for multiple cell nuclei per condition.

Microscopy imaging

Confocal imaging of immunostained emerin in normal HDF, emerin-null HDF and emerin null HDF after expression of wild-type PA-TagRFP-emerin were performed on an Olympus Fluoview FV1000 confocal microscope equipped with a 60x/1.40 NA objective, 405 nm and 488 nm lasers and appropriate emission filters for imaging DAPI (450/20 nm) and Alexa-488 labeled antibodies against emerin (510/10 nm).

Confocal imaging of nuclear deformation and actin organization in micropatterned $EMD^{+/y}$ HDF was performed on a Zeiss LSM 700 microscope equipped with a C-Apochromat 63×/1.15 W Korr objective, excitation lasers at 405 nm and 488 nm and appropriate beamsplitter and emission channel settings for dual detection of DAPI and phalloidin-iFluor 488.

Wide-field imaging of labeled actin and labeled nuclei for NSI measurements were performed on an inverted Nikon Eclipse Ti-E microscope equipped with a 40x objective (Nikon), an iXon Ultra

EMCCD camera (Andor), 405 nm and 488 nm lasers, a T495lpxr dichroic mirror and a 525/50 emission filter (Chroma) for phalloidin-iFluor 488 or a 458Di02 dichroic mirror and a 483/32 emission filter (Semrock) for DAPI.

SptPALM, dSTORM and CALM imaging were performed on an inverted Nikon Eclipse Ti-E microscope equipped with a 100x 1.49 NA objective (Nikon), an iXon EMCCD camera (Andor), perfect focus drift compensation optics, an astigmatic lens for 3D super-resolution imaging, a piezo z-scanner for calibration of 3D super-resolution images (Mad City Labs), laser lines at 405, 488, 561 and 647 nm (Agilent), a multiband pass ZET405/488/561/647x excitation filter (Chroma), a quad-band ZT405/488/561/647 dichroic mirror (Chroma) and appropriate emission filters for sptPALM imaging of PA-tagRFP (600/50 nm, Chroma), 3D-dSTORM imaging of Alexa-647 (700/75 nm, Chroma) and CALM imaging of complemented split-GFP (525/50 nm, Semrock).

sptPALM of PA-TagRFP-emerin was performed in 37ºC HBSS buffer (Corning) by HILO excitation of the bottom nuclear membrane of cells with a continuous and low power photoactivation at 405 nm and an excitation at 561 nm. The HILO illumination angle was θ= 51.6º. Images were acquired continuously at a frame rate of 40 ms/frame for no longer than 3 minutes per cell to limit UV damage. CALM imaging of complemented emerin-GFP-emerin species was done as described for sptPALM but with a single HILO excitation at 488 nm.

dSTORM of SNAP-emerin labeled with BG-A647 was performed at room temperature in a photoswitching buffer composed of 10% glucose, 0.5 mg/ml glucose oxidase (Sigma), 40 μg/ml catalase (Sigma), and 1% β-mercaptoethanol (Sigma). Continuous photoswitching was achieved with a low power 488 nm laser and imaging was done with a 647 nm laser excitation at a frame rate of 80 ms/frame. Z-calibration and sample drift corrections were done using a few 40 nm TransFluoSphere beads (488/685 nm, Life Technologies) as fiducial markers spread on the cell samples.

Analyses of diffusion coefficients

Localization and tracking analyses were performed using the software package SLIMfast, which uses multiple-target tracing algorithms[57] and was kindly provided by Christian Ritcher and Jacob Piehler. Localizations were performed by 2D-gaussian fitting of the point-spread-function of each activated PA-TagRFP-emerin or activated emerin-GFP-emerin species in each frame. Localization precision was determined as previously described[58], and individual PA-TagRFP-emerin were localized with a precision of 13±5 nm. Diffusion trajectories were built by linking localizations frame to frame and accounting for blinking statistics and local particle densities. Trajectories with fewer than three steps were discarded. Diffusion coefficients were estimated using a probability density of square displacement (PDSD) analysis[35]. For each time lag t, the PDSD curve was fitted with the following model:

$$P(\vec{r}^2, t) = 1 - \sum_{i=1}^{n} a_i(t)e^{-r^2/r_i^2(t)} \qquad (2)$$
$$\sum_{i=1}^{n} a_i(t) = 1$$

where $r_i^2(t)$ is the square displacement and $a_i(t)$ is the population density of i numbers of diffusive behaviors at each time lag t. To limit the risks of overfitting or underfitting the PDSD curves and select an appropriate model for i numbers of diffusive behaviors in each data set, we used both an Akaike information criterion (AIC) and a Bayesian information criterion (BIC) after fitting PDSD with models where $1 \leq i \geq 5$. Square displacement curves ($r_i^2(t)$) were extracted from PDSD

analyses and reported with error bars determined using $\frac{r_i^2}{\sqrt{N}}$, where N is the number of analyzed trajectories per time lag, as previously described[35]. Diffusion coefficients (D) representative of each behaviors were determined by fitting each $r_i^2(t)$ curves over the first four time lags (t_1-t_4) using OriginPro 2020 software (OriginLab) and a 2D Brownian diffusion model with position error:

$$r^2 = 4Dt + 4\sigma^2 \qquad (3)$$

All diffusion coefficients D are reported in µm^2/s ± standard error of fit value (± s.e.m.). Statistical comparisons between D values were done using F-tests. Population percentages are derived from the averaged $a_i(t)$ values over the considered time lags.

Individual diffusion coefficients (D_i) were obtained by fitting the individual mean square displacement (MSD) for each detected emerin over the first three time lags (t_1-t_3), using again a 2D Brownian diffusion model. Based on their individual D_i value, emerin trajectories were grouped into four diffusion ranges ($D_{i1}> 0.1$ µm^2/s, $0.1<D_{i2}> 0.01$ µm^2/s, $0.1<D_{i3}> 0.001$ µm^2/s, and $D_{i4}< 0.001$ µm^2/s) and plotted as maps.

Spatial distribution and cluster analyses from super-resolution images

After 3D-dSTORM super-resolution imaging, the localization of individual emerin molecules and z-position assignments were performed by Gaussian fitting using rapidSTORM (version 3.3.1)[59]. Sample drift and overcounting corrections for molecules appearing in consecutive frames were done using PALMsiever[60] and renderings of super-resolved images were done using ImageJ[55]. Localization precisions (σ) in the x, y, and z dimensions were evaluated as previously described[32] and were σ_x:8.3 nm, σ_y:13.0 nm, and σ_z:28.4 nm. 2D spatial pattern analyses of emerin distributions were performed on 2 µm x 2 µm regions of interest (ROI) typically chosen in nuclear envelope areas having homogenous z ranges and away from the edges of nuclei, in order to limit 3D effects. Emerin clustering was determined using an edge-corrected neighborhood density function (NDF) as previously described[32]. Briefly, the NDF is a pairwise-correlation function similar to O-ring statistics that tallies the density of detected emerin within a ring of outer radius r and width Δr located at a distance r from an emerin position in the ROI and for all $r + \Delta r$ in the ROI. The density of emerin as a function of distance from an average emerin was obtained with:

$$D_r = \frac{\sum N_r}{\sum A_r} \qquad (4)$$

where N_r is the number of neighbors and A_r is the area summed over all detected emerin. NDF analyses were done over a 1µm distance on selected ROIs and with a fixed ring width of 10 nm and a ring radius increasing by 10 nm steps. To average NDF statistics from multiple ROIs across different nuclei and make them sample-size independent, D_r was further standardized by dividing it by the mean density of detected emerin across the entire ROI. As such, an NDF value at a given radius indicates the relative clustering of emerin as compared to the average density across the entire sample. This relative NDF gives a value of 1 for a completely random spatial distribution as determined by Monte Carlo simulations of random emerin distributions with area and number of randomly seeded emerin equal to that of each experimental ROIs.

Relative NDF curves averaged across multiple ROIs and multiple nuclei were fitted with a previously described model[32], which accounts for a distribution of cluster lengths that includes two populations of emerin (monomer and oligomers) and for a probability density of emerin in 2D clusters that decays approximately as an exponential function[45]:

22

$$\text{Relative NDF} = \{A_1 \times \exp\left(\frac{-r}{\varepsilon_1}\right) + A_2 \times \exp\left(\frac{-r}{\varepsilon_2}\right) + 1\} * g(r)^{PSF} \quad (5)$$

where, A is the clustering density, ε is the typical half-maximum cluster length, $*$ denotes a 2D convolution, and $g(r)^{PSF}$ is the correlation function of the effective point spread function of uncertainty in position determination for the dSTORM experiments. As described previously[32], $g(r)^{PSF}$ corrects the NDF for contribution of multiple single molecule appearances (blinking) to the overall spatial distribution. After fitting relative NDF curves, the molecular density above random for emerin clusters are reported as $A \pm$ standard error of the fit ($\pm$s.e.m) and their typical length scales as $2 \times \varepsilon \pm$ standard error of the fit and localization precision ($\pm$s.e.m). Relative increases in emerin oligomer formation during nuclear stress were determined by considering a circular shape of oligomer nanodomains and multiplying the area of oligomerization by the measured molecular density.

Cluster maps

Cluster maps were generated from drift- and overcounting-corrected super-resolved emerin positions by determining local cluster values around each emerin using the Getis and Franklin L function[46] in spPack[61] and for a distance of 25 nm. Spatial positions in x and y, and cluster values were plotted as maps in MATLAB (MathWorks) using the meshgrid and griddata functions, a 1 nm x 1 nm pixel size and the 'v4' option when calculating pixel density values. The contour maps were generated using the countourf function with 200 levels. In contour maps, values $L(r_{25})=25$ represent areas where emerin is randomly distributed and $L(r_{25})=70$ values represent areas with emerin local density $(70/25)^2 = \sim$8-fold higher than expected for a random distribution.

ACKNOWLEDGMENTS

AUTHOR CONTRIBUTIONS

A.F. and M.B. designed and performed experiments, contributed reagents and analyses, and participated in writing of the manuscript. F.P. conceived and supervised the research, designed and performed experiments, contributed analyses and wrote the manuscript.

COMPETING FINANCIAL INTERESTS

The authors declare no competing financial interests
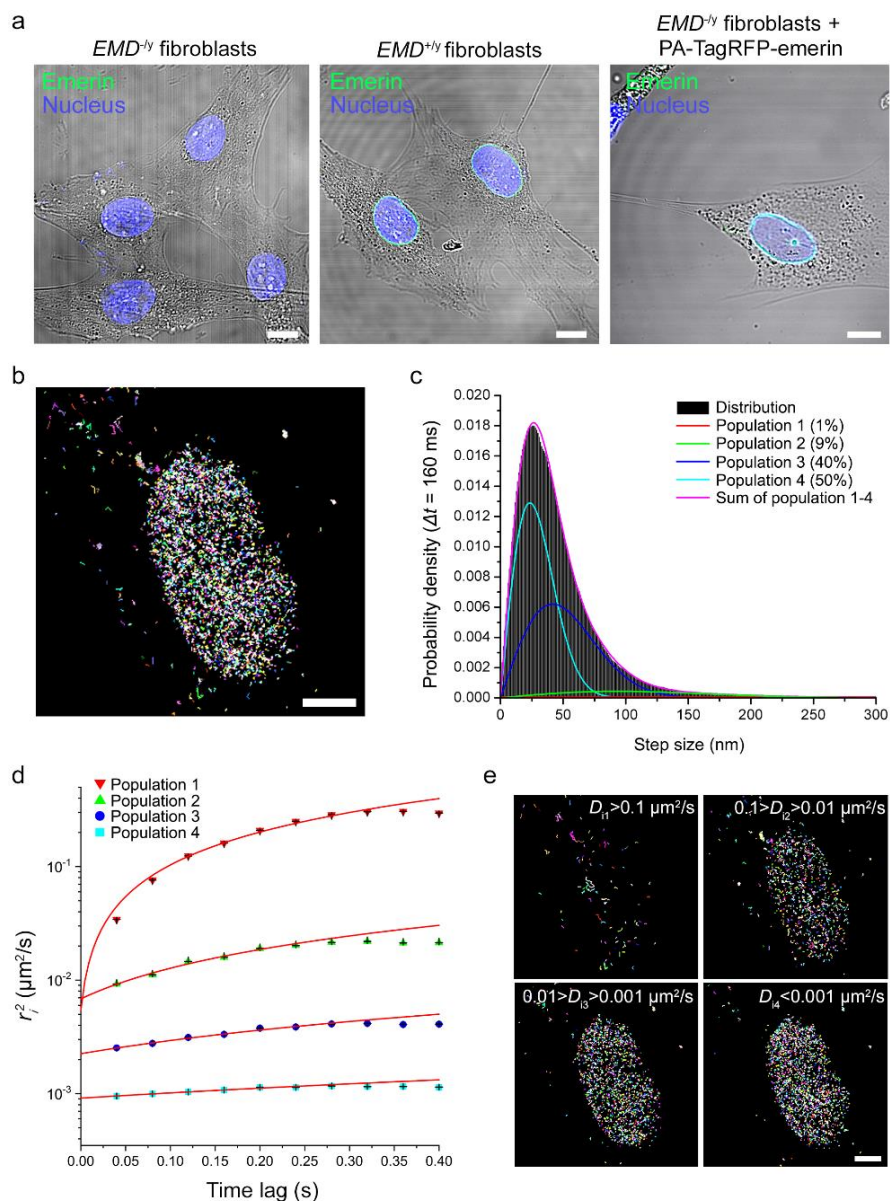
Figure 1

Figure 1. Emerin displays four distinct diffusive behaviors at endoplasmic reticulum membrane and the nuclear envelope. a) Immunostaining and confocal imaging of emerin in emerin-null HDF ($EMD^{-/y}$), HDF with endogenous emerin expression ($EMD^{+/y}$) and $EMD^{-/y}$ HDF after expression of wild-type PA-TagRFP-emerin. Scale: 10 µm. b) Map of emerin trajectories built from localization and tracking of individual PA-TagRFP-emerin at the bottom nuclear envelope. Scale: 5 µm. c) Probability distribution of square displacement (PDSD) for wild-type emerin (71004 trajectories in 14 cells) at time lag $\Delta t = 160$ ms. The distribution is composed of four diffusive behaviors. d) Square displacement curves (r^2_i) for each emerin diffusive behavior generated from PDSD analyses on the first ten time lags Δt 40-400 ms. Curves are fitted over the first four values with a Brownian diffusion model (red line) to estimate the respective diffusion coefficients of each emerin behaviors. e) Separated emerin trajectory maps as a function of individual diffusion coefficient (D_i). Scale: 5 µm.
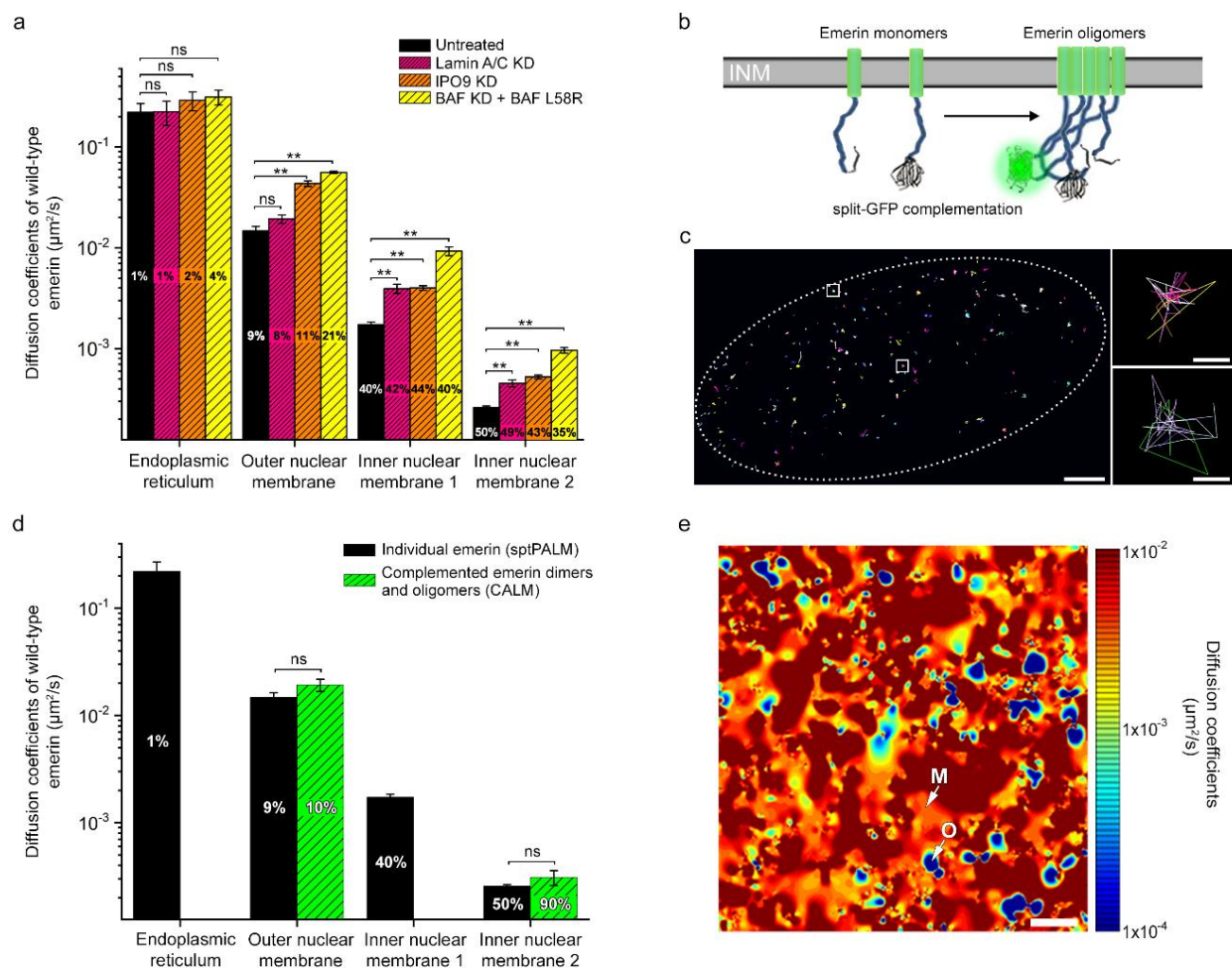
24

Figure 2

Figure 2. Emerin diffuses as inner nuclear membrane monomers and oligomers that interact with lamin A/C, nuclear actin and BAF. a) Diffusion coefficients (± s.e.m.) and population percentages of wild-type emerin (untreated, n=71004 trajectories in 14 nuclei) after depletion of lamin A/C (lamin A/C KD, n=60569 trajectories in 11 nuclei), depletion of nuclear actin (IPO9 KD, n=74501 trajectories in 17 nuclei) or replacement of endogenous BAF with BAF L58R mutant (BAF KD + BAF L68R, n=62714 trajectories in 8 nuclei) (F-test, ns: non-significant, **: p<0.01). b) Schematic of emerin fused to complementary split-GFP fragments and co-expressed to track the mobility of emerin oligomers by single molecule imaging of complemented GFP. c) Map of individual trajectories for complemented emerin-GFP-emerin species at the nuclear envelope (left) and examples of oligomer domains (squares) where trajectories often overlap (left). Scales: 2 µm (left) and 50 nm (right). d) Comparison of diffusion coefficients (± s.e.m.) and population percentages for individual wild-type emerin assessed by sptPALM and complemented emerin-GFP-emerin species (n=4833 trajectories in 13 nuclei) assessed by CALM (F-test, ns: non-significant). e) Diffusion map of wild-type PA-TagRFP-emerin at the nuclear envelope where emerin oligomers form slow mobility domains (blue, O) surrounded by larger areas where emerin monomers diffuse faster (red, M). Scale: 500 nm.
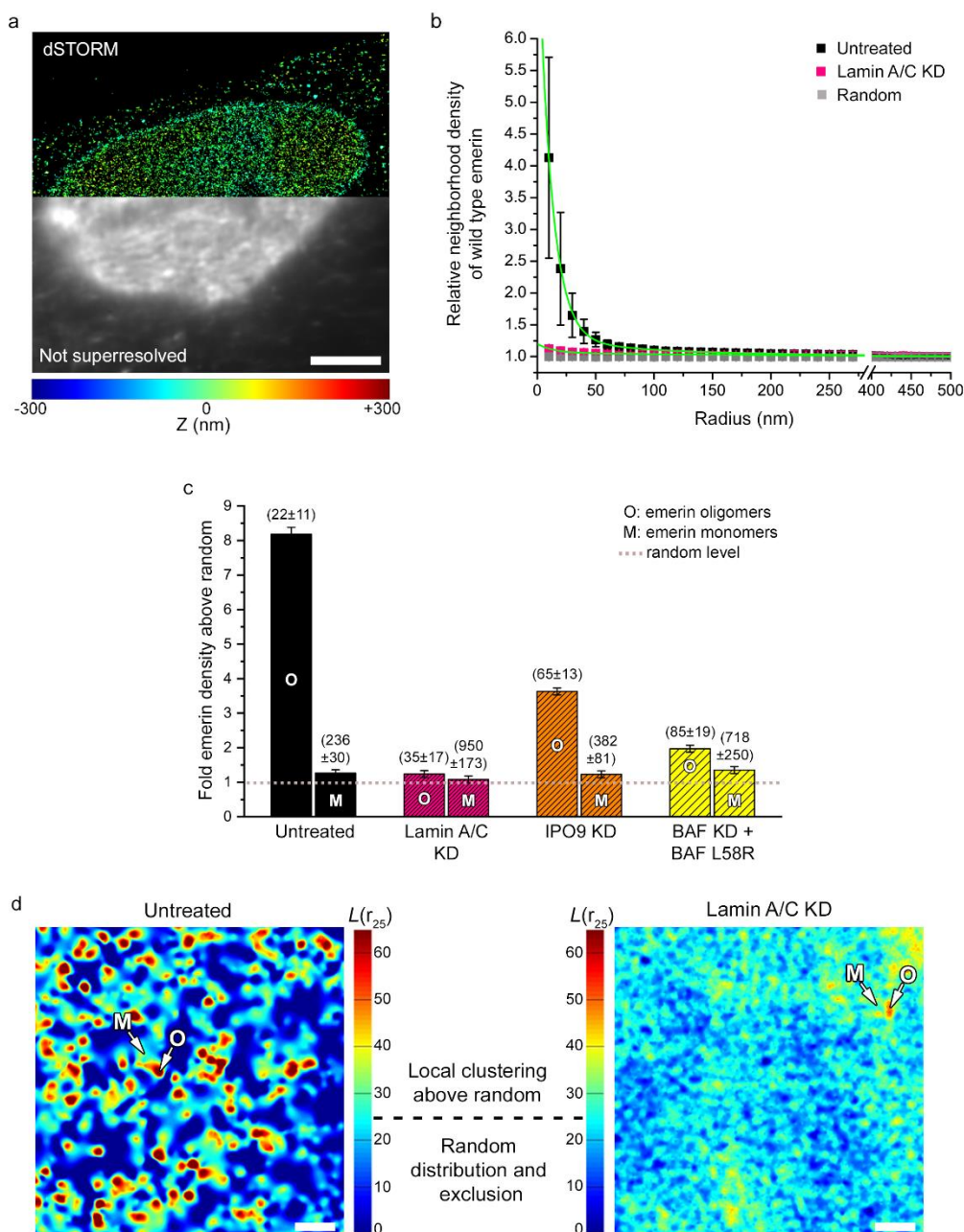
25

Figure 3

Figure 3. Emerin forms oligomeric nanodomains stabilized by lamin A/C and surrounded by larger emerin monomer areas across the nuclear membrane. a) Super-resolved 3D-dSTORM positions (top half) and non-super-resolved imaging (bottom half) of wild-type SNAP-emerin at the bottom nuclear envelope of an *EMD*$^{-/y}$ HDF. Scale: 5 µm. b) Neighborhood densities (± s.d.) and cluster analyses of wild-type emerin at the nuclear membrane of untreated HDF (n=189,331 localizations in 10 nuclei) and HDF after lamin A/C knock down (n=178,206 localizations in 6 nuclei). Neighborhood densities at various length scales are compared to MonteCarlo simulations of complete spatial randomness and fitted to measure molecular densities above random and length scale of significant clustering (green). c) Relative nuclear envelope molecular densities above random (± s.e.m.) for wild-type emerin oligomers (O) and monomers (M) in untreated *EMD*$^{-/y}$

HDF, HDF depleted for lamin A/C, HDF depleted for nuclear actin after IPO9 knock down (n=225,394 localizations in 9 nuclei) and HDF where endogenous BAF is replaced by BAF L58R (n=90,241 localizations in 6 nuclei). Values in parenthesis represent the typical length scale (± s.e.m.) of each domain in nanometers. d) Local cluster maps of wild-type emerin in nuclear envelope regions of untreated (left) and lamin A/C knocked down HDF (right) for a search radius of 25 nm ($L(r_{25})$). Cluster values in maps are assigned to all localized emerin, where values $L(r_{25})=25$ represent areas where emerin is randomly distributed and $L(r_{25})=70$ values represent areas with emerin local densities $(70/25)^2 = {\sim}8$-fold higher than expected for a random distribution. M: monomer areas, O: oligomer nanodomains. Scale: 250 nm.
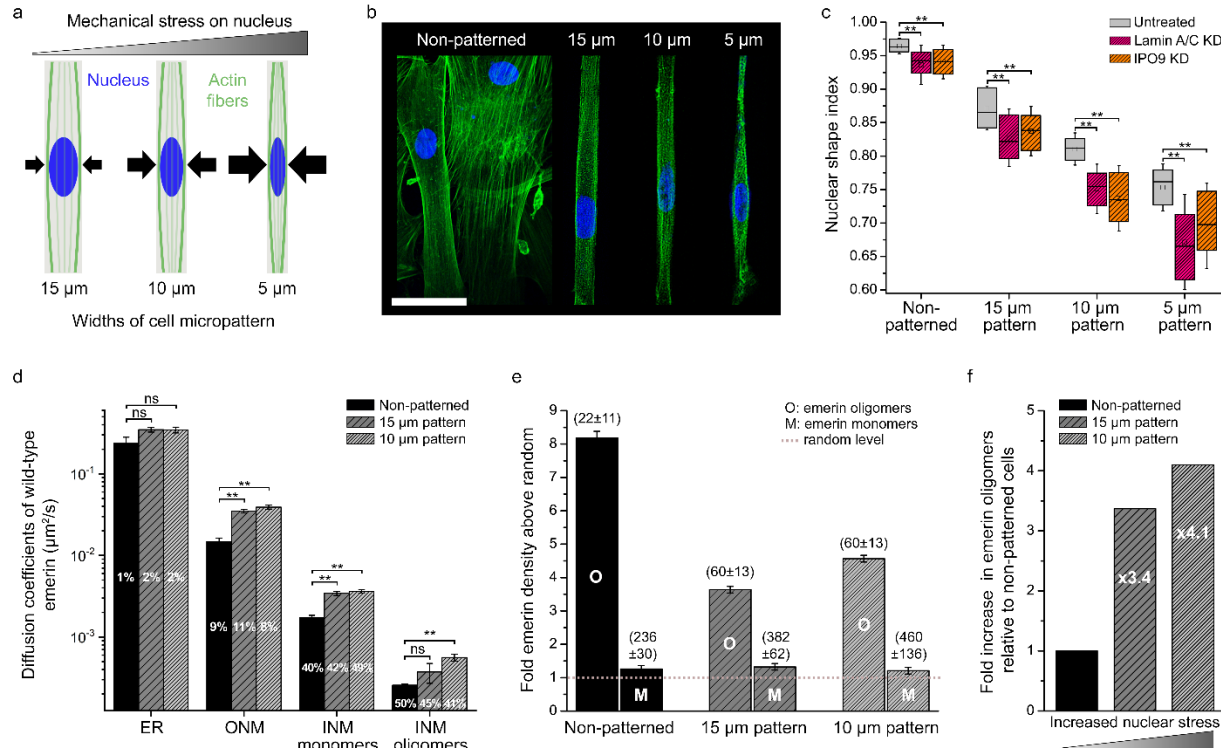
Figure 4

Figure 4. Mechanical stress on the nucleus increases emerin mobility and the formation of emerin oligomers. a) Schematic for increasing mechanical stress on the nucleus by cell micropatterning on rectangular fibronectin strips with decreasing widths of 15, 10 and 5 µm. Arrows represent forces. b) Fluorescence confocal imaging of actin (green) and the nucleus (blue) in micropatterned *EMD*[+/y] HDF. Scale: 50 µm. c) Nuclear shape index as a function of micropattern width for untreated *EMD*[+/y] HDF (n=54, 70, 61 and 62 nuclei for non-patterned, 15, 10 and 5 µm wide patterns, respectively), HDF depleted for lamin A/C (n=75, 60, 70 and 66 nuclei) and HDF depleted for nuclear actin (n=62, 71, 66 and 46 nuclei). Box length: index interquartile range; central square: mean; central bar: median; error bars: ± s.d. (T-test, ** p < 0.01). d) Diffusion coefficients (± s.e.m.) and population percentages of wild-type emerin in non-patterned cells or after nuclear deformation on 15 µm wide (*n=27266* trajectories in 10 nuclei) and 10 µm wide micropatterns (*n=12915* trajectories 8 nuclei) (F-test, ns: non-significant, **: *p<0.01*. e) Relative nuclear envelope molecular densities above random (± s.e.m.) for wild-type emerin oligomers (O) and monomers (M) in non-patterned *EMD*[-/y] HDF or after nuclear deformation on 15 µm wide (n=151,647 localizations in 10 nuclei) or 10 µm wide micropatterns (n=56,563 localizations in 6 nuclei). Values in parenthesis represent the typical length scale (± s.e.m.) of each domain in nanometers. f) Increase in emerin oligomers as a function of nuclear stress on 15 and 10 µm wide micropatterns compared to non-deformed nuclei in non-patterned cells.
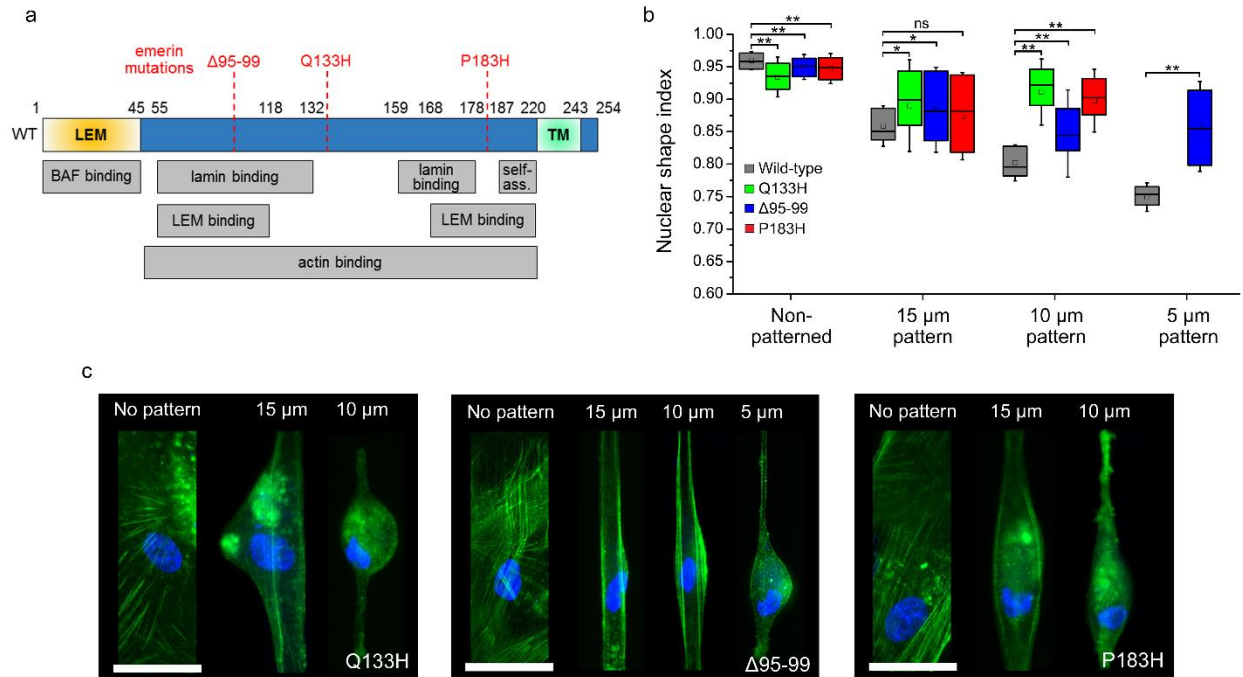
28

Figure 5

Figure 5. Emerin mutations induce defective nuclear shape adaptation against mechanical stress. a) Diagram of wild-type emerin (WT) showing its transmembrane (TM) and LEM domains, its disordered central region with relevant binding domains and self-association domain (self-ass.) and the position of Δ95-99, Q133H and P183H EDMD-inducing mutations. b) Nuclear shape index as a function of micropattern width for *EMD*$^{-/y}$ HDF expressing wild-type emerin (n=38, 33, 26 and 57 nuclei for non-patterned, 15, 10 and 5 µm wide patterns, respectively), Q133H emerin (n= 74, 58 and 37 nuclei), Δ95-99 emerin (n= 64, 89, 45 and 46 nuclei) and P183H emerin (n=82, 78 and 28 nuclei). Box length: index interquartile range; central square: mean; central bar: median; error bars: ± s.d. (T-test, ns: non-significant, *: *p*<0.05, **: *p*<0.01. c) Fluorescence wide-field imaging of actin (green) and the nucleus (blue) in micropatterned *EMD*$^{-/y}$ HDF expressing Q133H, Δ95-99 or P183H emerin mutants. Scales: 50 µm.
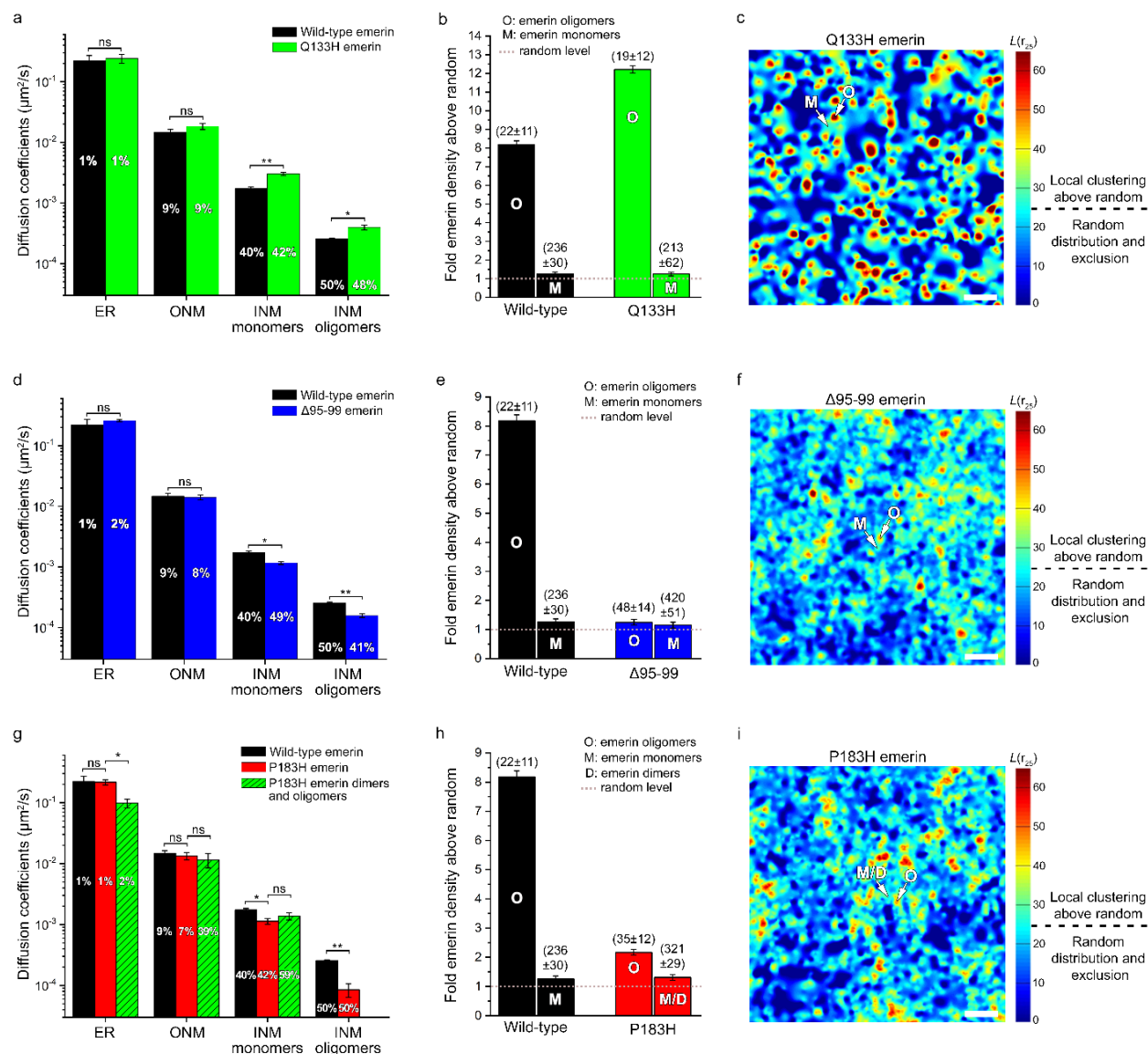
Figure 6

Figure 6. Emerin mutants exhibit modified lateral mobilities and defective oligomerization at the inner nuclear membrane. a) Diffusion coefficients (± s.e.m.) and population percentages of Q133H emerin (*n*=105050 trajectories in 13 nuclei) compared to wild-type emerin (n=71004 trajectories in 14 nuclei) (F-test, ns: non-significant, *: *p*<0.05, **: *p*<0.01). b) Relative nuclear envelope molecular densities above random (± s.e.m.) for Q133H emerin oligomers (O) and monomers (M) (n=149,340 localizations in 6 nuclei) compared to wild-type emerin (n=189,331 localizations in 10 nuclei). c) Local cluster map of Q133H emerin at the nuclear envelope for a search radius of 25 nm (*L*(r$_{25}$)). M: monomer areas, O: oligomer nanodomains. Scale: 250 nm. d) Diffusion coefficients (± s.e.m.) and population percentages of Δ95-99 emerin (*n*=76944 trajectories in 14 nuclei) compared to wild-type emerin (F-test, ns: non-significant, *: *p*<0.05, **: *p*<0.01. e) Relative nuclear envelope molecular densities above random (± s.e.m.) for Δ95-99 emerin oligomers (O) and monomers (M) (n=208,092 localizations in 8 nuclei) compared to wild-type emerin. f) Local cluster map of Δ95-99 emerin. M: monomer areas, O: oligomer nanodomains.

30

Scale: 250 nm. g) Diffusion coefficients (± s.e.m.) and population percentages of P183H emerin (n=86529 trajectories in 21 nuclei) compared to wild-type emerin and compared to complemented P183H emerin-GFP-emerin species (n=10519 trajectories in 21 nuclei) assessed by CALM (F-test, ns: non-significant, *: p<0.05, **: p<0.01). h) Relative nuclear envelope molecular densities above random (± s.e.m.) for P183H emerin oligomers (O) and monomers/dimers (M/D) (n=138,075 localizations in 6 nuclei) compared to wild-type emerin. i) Local cluster map of P183H emerin. M/D: monomer/dimer areas, O: oligomer nanodomains. Scale: 250 nm. Values in parenthesis in b, e and h represent the typical length scale (± s.e.m.) of each domain in nanometers.
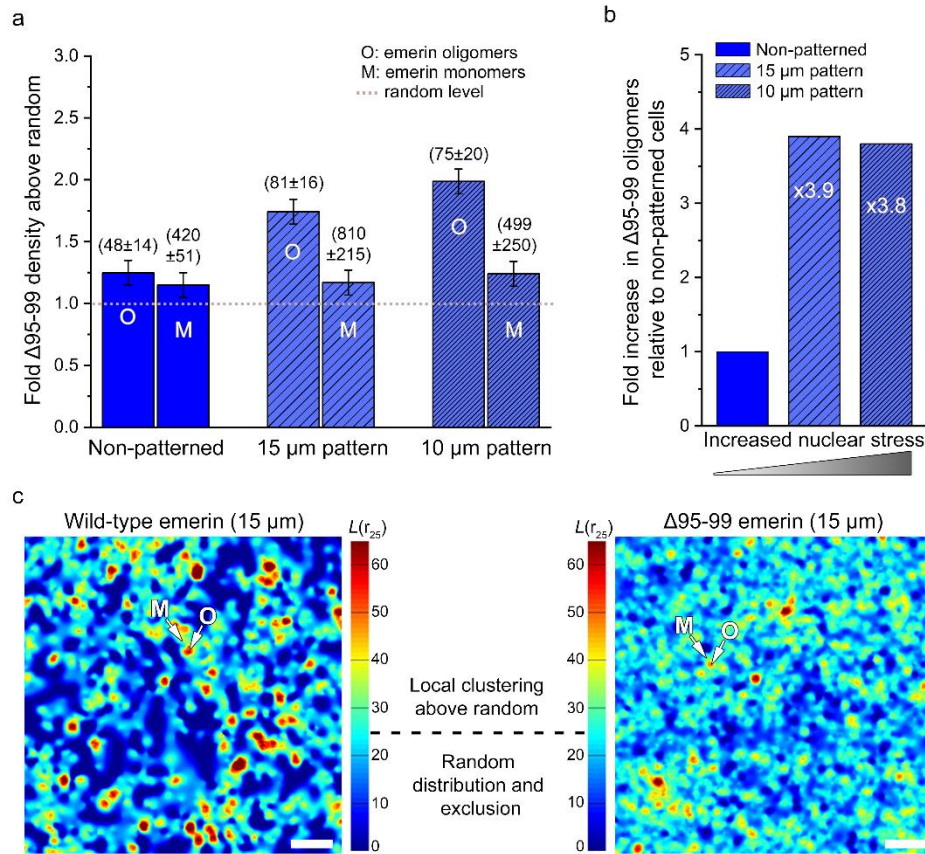
Figure 7

Figure 7. Insufficient oligomerization of EDMD-inducing Δ95-99 emerin mutant against mechanical stress. a) Relative nuclear envelope molecular densities above random (± s.e.m.) for Δ95-99 emerin oligomers (O) and monomers (M) in non-patterned $EMD^{-/y}$ HDF or after nuclear deformation on 15 µm wide (n=138,119 localizations in 5 nuclei) or 10 µm wide micropatterns (n=135,143 localizations in 6 nuclei). Values in parenthesis represent the typical length scale (± s.e.m.) of each domain in nanometers. b) Increase in Δ95-99 emerin oligomers as a function of nuclear stress on 15 and 10 µm wide micropatterns compared to non-deformed nuclei in non-patterned cells. c) Local cluster maps of wild-type and Δ95-99 emerin after nuclear deformation on 15 µm wide micropatterns. M: monomer areas, O: oligomer nanodomains. Scale: 250 nm.

REFERENCES

1. Berk, J.M., Tifft, K.E. & Wilson, K.L. The nuclear envelope LEM-domain protein emerin. *Nucleus* **4**, 298-314 (2013).

2. Kirby, T.J. & Lammerding, J. Emerging views of the nucleus as a cellular mechanosensor. *Nat. Cell Biol.* **20**, 373-381 (2018).

3. Cui, Y. *et al.* Cyclic stretching of soft substrates induces spreading and growth. *Nat. Commun.* **6**, 6333 (2015).

4. Demmerle, J., Koch, A.J. & Holaska, J.M. The nuclear envelope protein emerin binds directly to histone deacetylase 3 (HDAC3) and activates HDAC3 activity. *The Journal of Biological Chemistry* **287**, 22080-22088 (2012).

5. Stephens, A.D., Banigan, E.J., Adam, S.A., Goldman, R.D. & Marko, J.F. Chromatin and lamin A determine two different mechanical response regimes of the cell nucleus. *Mol. Biol. Cell* **28**, 1984-1996 (2017).

6. Maurer, M. & Lammerding, J. The Driving Force: Nuclear Mechanotransduction in Cellular Function, Fate, and Disease. *Annu. Rev. Biomed. Eng.* **21**, 443-468 (2019).

7. Emery, A.E. Emery-Dreifuss muscular dystrophy - a 40 year retrospective. *Neuromuscul. Disord.* **10**, 228-232 (2000).

8. Emery, A.E. & Dreifuss, F.E. Unusual type of benign x-linked muscular dystrophy. *J Neurol Neurosurg Psychiatry* **29**, 338-342 (1966).

9. Maggi, L., Carboni, N. & Bernasconi, P. Skeletal Muscle Laminopathies: A Review of Clinical and Molecular Features. *Cells* **5** (2016).

10. Frock, R.L. *et al.* Lamin A/C and emerin are critical for skeletal muscle satellite cell differentiation. *Genes Dev.* **20**, 486-500 (2006).

11. Fidzianska, A. & Hausmanowa-Petrusewicz, I. Architectural abnormalities in muscle nuclei. Ultrastructural differences between X-linked and autosomal dominant forms of EDMD. *J. Neurol. Sci.* **210**, 47-51 (2003).

12. Park, Y.-E. *et al.* Nuclear changes in skeletal muscle extend to satellite cells in autosomal dominant Emery-Dreifuss muscular dystrophy/limb-girdle muscular dystrophy 1B. *Neuromuscul. Disord.* **19**, 29-36 (2009).

13. Rowat, A.C., Lammerding, J. & Ipsen, J.H. Mechanical properties of the cell nucleus and the effect of emerin deficiency. *Biophys. J.* **91**, 4649-4664 (2006).

14. Lammerding, J. *et al.* Abnormal nuclear shape and impaired mechanotransduction in emerin-deficient cells. *J. Cell Biol.* **170**, 781-791 (2005).

15. Yuan, J. & Xue, B. Role of structural flexibility in the evolution of emerin. *J. Theor. Biol.* **385**, 102-111 (2015).

16. Clements, L., Manilal, S., Love, D.R. & Morris, G.E. Direct interaction between emerin and lamin A. *Biochemical and Biophysical Research Communications* **267**, 709-714 (2000).

17. Sakaki, M. *et al.* Interaction between emerin and nuclear lamins. *Journal of Biochemistry* **129**, 321-327 (2001).

18. Berk, J.M. *et al.* The molecular basis of emerin-emerin and emerin-BAF interactions. *J. Cell Sci.* **127**, 3956-3969 (2014).

19. Fairley, E.A., Kendrick-Jones, J. & Ellis, J.A. The Emery-Dreifuss muscular dystrophy phenotype arises from aberrant targeting and binding of emerin at the inner nuclear membrane. *J. Cell Sci.* **112**, 2571-2582 (1999).

20. Lee, K.K. *et al.* Distinct functional domains in emerin bind lamin A and DNA-bridging protein BAF. *J. Cell Sci.* **114**, 4567-4573 (2001).

21. Mislow, J.M.K. *et al.* Nesprin-1α self-associates and binds directly to emerin and lamin A in vitro. *FEBS Lett.* **525**, 135-140 (2002).

22. Haque, F. *et al.* Mammalian SUN protein interaction networks at the inner nuclear membrane and their role in laminopathy disease processes. *J. Biol. Chem.* **285**, 3487-3498 (2010).

23. Herrada, I. *et al.* Muscular Dystrophy Mutations Impair the Nuclear Envelope Emerin Self-assembly Properties. *ACS Chem. Biol.* **10**, 2733-2742 (2015).

24. Samson, C. *et al.* Emerin self-assembly mechanism: role of the LEM domain. *FEBS J.* **284**, 338-352 (2017).

25. Roberts, R.C. *et al.* The Emery-Dreifuss muscular dystrophy associated-protein emerin is phosphorylated on serine 49 by protein kinase A. *FEBS J.* **273**, 4562-4575 (2006).

26. Berk, J.M. *et al.* O-Linked beta-N-acetylglucosamine (O-GlcNAc) regulates emerin binding to barrier to autointegration factor (BAF) in a chromatin- and lamin B-enriched "niche". *J. Biol. Chem.* **288**, 30192-30209 (2013).

27. Guilluy, C. *et al.* Isolated nuclei adapt to force and reveal a mechanotransduction pathway in the nucleus. *Nat. Cell Biol.* **16**, 376-381 (2014).

28. Hirano, Y. *et al.* Dissociation of Emerin from Barrier-to-autointegration Factor Is Regulated through Mitotic Phosphorylation of Emerin in a Xenopus Egg Cell-free System. *J. Biol. Chem.* **280**, 39925-39933 (2005).

29. Yates, J.R. & Wehnert, M. The Emery-Dreifuss Muscular Dystrophy Mutation Database. *Neuromuscul. Disord.* **9**, 199 (1999).

30. Ellis, J.A., Craxton, M., Yates, J.R. & Kendrick-Jones, J. Aberrant intracellular targeting and cell cycle-dependent phosphorylation of emerin contribute to the Emery-Dreifuss muscular dystrophy phenotype. *J. Cell Sci.* **111**, 781-792 (1998).

31. Holt, I., Clements, L., Manilal, S. & Morris, G.E. How does a g993t mutation in the emerin gene cause Emery-Dreifuss muscular dystrophy? *Biochemical and Biophysical Research Communications* **287**, 1129-1133 (2001).

32. Fernandez, A., Bautista, M., Stanciauskas, R., Chung, T. & Pinaud, F. Cell-Shaping Micropatterns for Quantitative Super-Resolution Microscopy Imaging of Membrane Mechanosensing Proteins. *ACS Appl Mater Interfaces* **9**, 27575-27586 (2017).

33. Talkop, U.A. *et al.* Early onset of cardiomyopathy in two brothers with X-linked Emery-Dreifuss muscular dystrophy. *Neuromuscul. Disord.* **12**, 878-881 (2002).

34. Tokunaga, M., Imamoto, N. & Sakata-Sogawa, K. Highly inclined thin illumination enables clear single-molecule imaging in cells. *Nat. Methods* **5**, 159-161 (2008).

35. Schutz, G.J., Schindler, H. & Schmidt, T. Single-molecule microscopy on model membranes reveals anomalous diffusion. *Biophys. J.* **73**, 1073-1080 (1997).

36. Ostlund, C., Ellenberg, J., Hallberg, E., Lippincott-Schwartz, J. & Worman, H.J. Intracellular trafficking of emerin, the Emery-Dreifuss muscular dystrophy protein. *J. Cell Sci.* **112**, 1709-1719 (1999).

37. Dopie, J., Skarp, K.P., Rajakyla, E.K., Tanhuanpaa, K. & Vartiainen, M.K. Active maintenance of nuclear actin by importin 9 supports transcription. *Proceedings of the National Academy of Sciences of the United States of America* **109**, E544-552 (2012).

38. Cabantous, S., Terwilliger, T.C. & Waldo, G.S. Protein tagging and detection with engineered self-assembling fragments of green fluorescent protein. *Nat. Biotechnol.* **23**, 102-107 (2005).

39. Pinaud, F. & Dahan, M. Targeting and imaging single biomolecules in living cells by complementation-activated light microscopy with split-fluorescent proteins. *Proceedings of the National Academy of Sciences* **108**, E201-E210 (2011).

40. Iino, R., Koyama, I. & Kusumi, A. Single Molecule Imaging of Green Fluorescent Proteins in Living Cells: E-Cadherin Forms Oligomers on the Free Cell Surface. *Biophys. J.* **80**, 2667-2677 (2001).

41. Samson, C. *et al.* Structural analysis of the ternary complex between lamin A/C, BAF and emerin identifies an interface disrupted in autosomal recessive progeroid diseases. *Nucleic Acids Res.* **46**, 10460-10473 (2018).

42. Burger, M., Schmitt-Koopmann, C. & Leroux, J.-C. DNA unchained: two assays to discover and study inhibitors of the DNA clustering function of barrier-to-autointegration factor. *Sci. Rep.* **10**, 12301 (2020).

43. Shimi, T. *et al.* Dynamic interaction between BAF and emerin revealed by FRAP, FLIP, and FRET analyses in living HeLa cells. *J. Struct. Biol.* **147**, 31-41 (2004).

44. Samwer, M. *et al.* DNA Cross-Bridging Shapes a Single Nucleus from a Set of Mitotic Chromosomes. *Cell* **170**, 956-972 e923 (2017).

45. Sengupta, P. *et al.* Probing protein heterogeneity in the plasma membrane using PALM and pair correlation analysis. *Nat. Methods* **8**, 969-975 (2011).

46. Getis, A. & Franklin, J. Second-Order Neighborhood Analysis of Mapped Point Patterns. *Ecology* **68**, 473-477 (1987).

47. Bautista, M., Fernandez, A. & Pinaud, F. A Micropatterning Strategy to Study Nuclear Mechanotransduction in Cells. *Micromachines* **10**, 810 (2019).

48. Folker, E.S. & Baylies, M.K. Nuclear positioning in muscle development and disease. *Front. Physiol.* **4**, 363 (2013).

49. Holaska, J.M., Kowalski, A.K. & Wilson, K.L. Emerin caps the pointed end of actin filaments: evidence for an actin cortical network at the nuclear inner membrane. *PLoS Biol.* **2**, E231 (2004).

50. Bengtsson, L. & Wilson, K.L. Multiple and surprising new functions for emerin, a nuclear membrane protein. *Curr. Opin. Cell Biol.* **16**, 73-79 (2004).

51. Ho, C.Y., Jaalouk, D.E., Vartiainen, M.K. & Lammerding, J. Lamin A/C and emerin regulate MKL1–SRF activity by modulating actin dynamics. *Nature* **497**, 507-511 (2013).

52. Tifft, K.E., Bradbury, K.A. & Wilson, K.L. Tyrosine phosphorylation of nuclear-membrane protein emerin by Src, Abl and other kinases. *J. Cell Sci.* **122**, 3780-3790 (2009).

53. Schreiner, S.M., Koo, P.K., Zhao, Y., Mochrie, S.G.J. & King, M.C. The tethering of chromatin to the nuclear envelope supports nuclear mechanics. *Nat. Commun.* **6**, 7159 (2015).

54. Stoynova, L., Solórzano, R. & Collins, E.D. Generation of large deletion mutants from plasmid DNA. *BioTechniques* **36**, 402-404, 406 (2004).

55. Schneider, C.A., Rasband, W.S. & Eliceiri, K.W. NIH Image to ImageJ: 25 years of image analysis. *Nat. Methods* **9**, 671-675 (2012).

56. Versaevel, M., Grevesse, T. & Gabriele, S. Spatial coordination between cell and nuclear shape within micropatterned endothelial cells. *Nature Communications* **3**, 671 (2012).

57. Serge, A., Bertaux, N., Rigneault, H. & Marguet, D. Dynamic multiple-target tracing to probe spatiotemporal cartography of cell membranes. *Nat. Methods* **5**, 687-694 (2008).

58. Thompson, R.E., Larson, D.R. & Webb, W.W. Precise nanometer localization analysis for individual fluorescent probes. *Biophys. J.* **82**, 2775-2783 (2002).

59. Wolter, S. *et al.* rapidSTORM: accurate, fast open-source software for localization microscopy. *Nat. Methods* **9**, 1040-1041 (2012).

60. Pengo, T., Holden, S.J. & Manley, S. PALMsiever: a tool to turn raw data into results for single-molecule localization microscopy. *Bioinformatics* **31**, 797-798 (2015).

61. Perry, G.L.W. SpPack: spatial point pattern analysis in Excel using Visual Basic for Applications (VBA). *Environ. Model. Software* **19**, 559-569 (2004).